small structures
www.small-structures.com

Structure and Kinetic Selectivity of Trapdoor Zeolites in Hydrogen Isotope Separation

Dankun Yang, Huan V. Doan, Shaoliang Guan, Ivan da Silva, Sebastien Rochat, Mi Tian, Thomas B. Scott, and Valeska P. Ting**

The potential of two families of trapdoor zeolites with chabazite (CHA) and merlinoite (MER) structures have been explored for selective hydrogen isotope separation by investigating the influence of framework structure and the presence of different trapdoor cations (K^+, Rb^+, and Cs^+) on the thermal and kinetic responses. By leveraging the distinct porous structures of these frameworks, the separation of H_2 and D_2 gases is facilitated. The energy required for hydrogen to displace the door-keeping cations and fully access the inner zeolite porosities is identified for each sample, with frameworks containing heavier cations requiring higher critical temperatures. At 77 K, both MER and CHA frameworks show D_2 adsorption amounts nearly double those of H_2. Kinetic studies indicate slower diffusion for D_2 molecules through these porous structures compared to H_2, particularly at pressures below 100 mbar. This research suggests that D_2 is more likely to access a broader range of diffusion pathways than H_2, due to the presence of the trapdoor cations restricting certain pathways during gas sorption. This leads to differing kinetic responses, increased adsorption amounts and prolonged equilibration times for D_2, indicating potential for effective separation of H_2 and D_2 using the molecular trapdoor mechanism.

1. Introduction

The shift toward renewable energy sources is crucial for advancing sustainable development goals. As the universe's most abundant element, hydrogen is fundamental to various eco-friendly energy strategies. Its isotopes, protium (H), deuterium (D) and tritium (T) are indispensable in applications such as moderators in different nuclear reactors[1,2] and critical inputs for nuclear fusion.[3] Despite their utility, separating and purifying hydrogen isotopes efficiently remain a formidable obstacle due to their close chemical and physical properties.[4] Deuterium and tritium occur naturally in extremely low concentrations, further complicating purification.[5] Traditional separation techniques, such as cryogenic distillation[6] and combined electrolysis-catalytic exchange,[7,8] demand significant energy inputs, undermining their feasibility from both economic and environmental perspectives.

To address these challenges, a wide range of materials and mechanisms have been explored for hydrogen isotope separation,

D. Yang, T. B. Scott
Interface Analysis Centre
School of Physics
University of Bristol
Bristol BS8 1TS, UK

H. V. Doan, V. P. Ting
Research School of Chemistry
Australian National University
Canberra ACT 2601, Australia
E-mail: XHuan.Doan@anu.edu.au; Valeska.Ting@anu.edu.au

S. Guan
Department of Materials Science and Metallurgy
University of Cambridge
Cambridge CB3 0FS, UK

The ORCID identification number(s) for the author(s) of this article can be found under https://doi.org/10.1002/sstr.202500211.

DOI: 10.1002/sstr.202500211

I. da Silva
ISIS Facility
STFC Rutherford Appleton Laboratory
Chilton, Oxfordshire OX11 0QX, UK

S. Rochat
School of Chemistry
University of Bristol
Bristol BS8 1TS, UK

S. Rochat
School of Engineering Mathematics and Technology
University of Bristol
Bristol BS8 1TS, UK

M. Tian
Department of Chemical Engineering
University of Bath
Bath BA2 7AY, UK

V. P. Ting
Department of Mechanical Engineering
University of Bristol
Bristol BS8 1TR, UK

each operating under distinct conditions with varying effectiveness. Palladium-based alloys, for example, offer high selectivity through strong chemical affinity but require high operating temperatures (above 300 °C) and substantial energy input.[9,10] In contrast, porous materials such as metal-organic frameworks (MOFs),[11,12] covalent organic frameworks (COFs),[13] porous organic cages (POCs),[14] nanoporous carbons,[15] and zeolites[16] have attracted increasing attention as energy-efficient alternatives, including kinetic quantum sieving (KQS) and chemical affinity-based interactions. Many of these systems demonstrate high isotope selectivity at cryogenic temperatures (often below 30 K),[17,18] but their practical deployment is limited by synthesis complexity, stability concerns, or the need for ultralow operating temperatures.

Within the broader category of porous materials, trapdoor zeolites offer a particularly promising pathway. These systems exhibit dynamic "trapdoor" behavior, in which extra-framework cations selectively regulate gas diffusion through eight-membered ring (8MR) windows.[19–22] Trapdoor zeolites such as chabazite (CHA) and merlinoite (MER) allow only molecules with high polarizability and quadrupole moments, such as CO_2, to diffuse with minimal energy barriers.[23–26] Other gases, like N_2, require additional thermal energy to displace these cations before passing through, introducing the concept of a critical temperature (T_c) for gas diffusion.[27,28] Earlier research centered on analyzing the structural dynamics of this mechanism under diverse thermal conditions and gas atmospheres, revealing how cation variations impact the uptake and diffusion of gases such as CO_2,[29,30] while these studies provided critical insights into framework flexibility, porosity modulation, and thermal responses in MER and CHA.[31–33]

These trapdoor zeolites offer promising potential for hydrogen isotope separation due to the pronounced differences in polarizability and cation displacement energy between H_2 and D_2. Compared to H_2, D_2 exhibits higher polarizability (2.4 times higher than H_2)[4,34] and lower required energy to dislocate the cation,[35,36] enabling it to more readily trigger the trapdoor mechanism and diffuse through the functional windows. These 8MR windows form during the synthesis of zeolites through different arrangements of four-membered rings (4MRs) and six-membered rings (6MRs),[37] which dictate the available diffusion pathways (**Figure 1**). While H_2 can only access these pathways above a certain threshold temperature, D_2 can do so at lower temperatures ($T < T_c$), enabling efficient isotope separation under controlled thermal conditions.

In addition to their performance, zeolites offer significant practical advantages over other porous materials such as MOFs. Zeolites possess exceptional thermal stability, typically withstanding temperatures above 600 °C, making them suitable for high-temperature processes and long-term industrial use.[38,39] They are also chemically robust in a wide range of environments, including humid and acidic conditions, where many MOFs tend to degrade. Furthermore, zeolites are produced at large scale using well-established, low-cost synthesis methods from earth-abundant precursors such as alumina and silica. In contrast, MOFs often require multistep synthesis, high-purity metal salts, and complex organic linkers, contributing to higher production costs and limited scalability. These factors make zeolites a more economically and operationally viable platform for large-scale hydrogen isotope separation applications.

In our earlier work, we investigated the thermal response of trapdoor structures in MER and CHA zeolites, revealing that adsorbed hydrogen alters crystalline responses at temperatures exceeding T_c. Through structural analysis under varying thermal conditions, we established that separation efficiency hinges on the synergy between framework geometry and cation dimensions.[18] This research advances earlier investigations by exploring hydrogen isotope separation in two families of trapdoor zeolites, with a particular emphasis on the kinetic diffusion and equilibrium adsorption behaviors of different isotopes. Unlike previous studies, which primarily focused on H_2 adsorption using breakthrough methods at temperatures above ambient, this work employs both rigorous isothermal adsorptions to determine the threshold conditions for H_2 and kinetic analyses to evaluate isotope-selective diffusion at liquid nitrogen

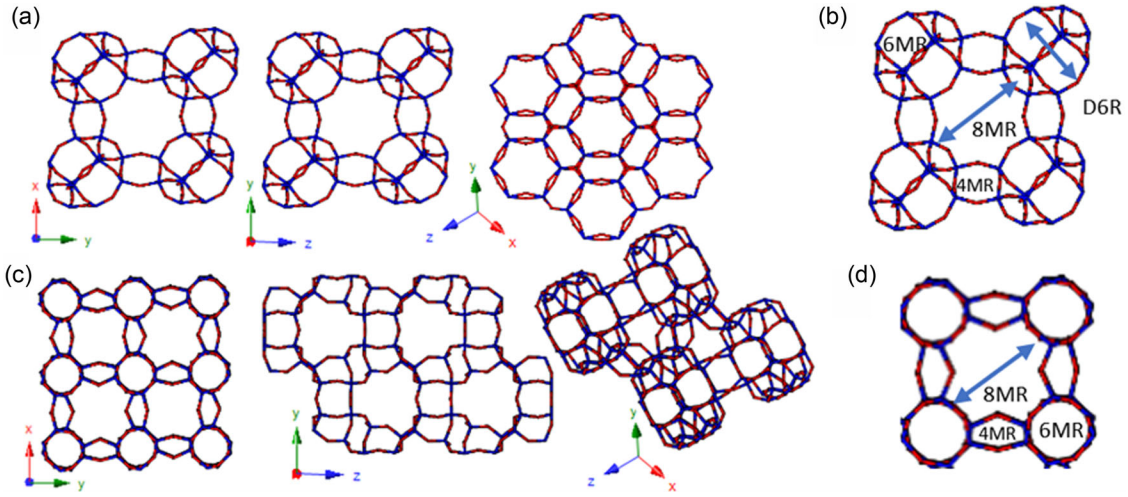

Figure 1. Illustrations depicting a) CHA framework structures viewed from different angles. b) Double six-membered rings (D6Rs), four-membered rings (4MRs), and eight-membered rings (8MRs) in CHA. c) MER framework structures viewed from different angles. d) Six-membered rings (6MRs), four-membered rings (4MRs), and eight-membered rings (8MRs) in MER. In these figures, Si—O bonds are represented in blue and Al—O bonds in red.

temperatures. The greater polarizability and stronger interactions of D_2 with trapdoor cations are predicted to facilitate its entry into the internal cavities of CHA and MER frameworks at cryogenic temperatures, offering a groundbreaking strategy for isotope separation. Furthermore, the study systematically examines how different cations (K^+, Rb^+, and Cs^+) impact separation efficiency through low-temperature (77 K) gas adsorption experiments. By integrating equilibrium and kinetic data, this work offers deeper mechanistic insight into isotope transport in trapdoor systems and highlights their potential for efficient, scalable separation technologies. Our findings establish a critical threshold for D_2 sorption at cryogenic temperatures and reveal how framework-cation interactions influence isotope selectivity. This research not only advances the practical utility of trapdoor zeolites for separating hydrogen isotopes but also offers a fresh kinetic perspective on molecular sieving processes. By linking fundamental insights into trapdoor mechanisms with actionable separation approaches, our research lays the groundwork for designing more efficient, scalable technologies in nuclear fuel refinement and hydrogen storage systems.

2. Results and Discussion

2.1. Elemental Composition and Distribution

The morphological features of the CHA and MER zeolite samples were previously characterized using scanning electron microscopy (SEM) and EDX analysis,[18] confirming uniform crystal structure and consistent elemental composition. Representative SEM images are provided in Figure S1a,b, Supporting Information. To further probe structural details, additional STEM analysis was conducted on CsCHA (Figure S1c,d, Supporting Information); however, due to the subnanometer dimensions of the functional trapdoor windows (≈4 Å), direct imaging of the extra-framework cations within the 8MRs was not feasible. As a result, STEM did not yield additional insights beyond SEM, and the trapdoor structure could not be resolved under currently available imaging conditions.

In this study, the chemical composition (**Figure 2**a) and elemental distribution (Figure 2b) of both CHA and MER frameworks were determined using X-ray photoelectron spectroscopy (XPS)[40,41] (refer to Figure 2 for CsMER, with other materials illustrated in

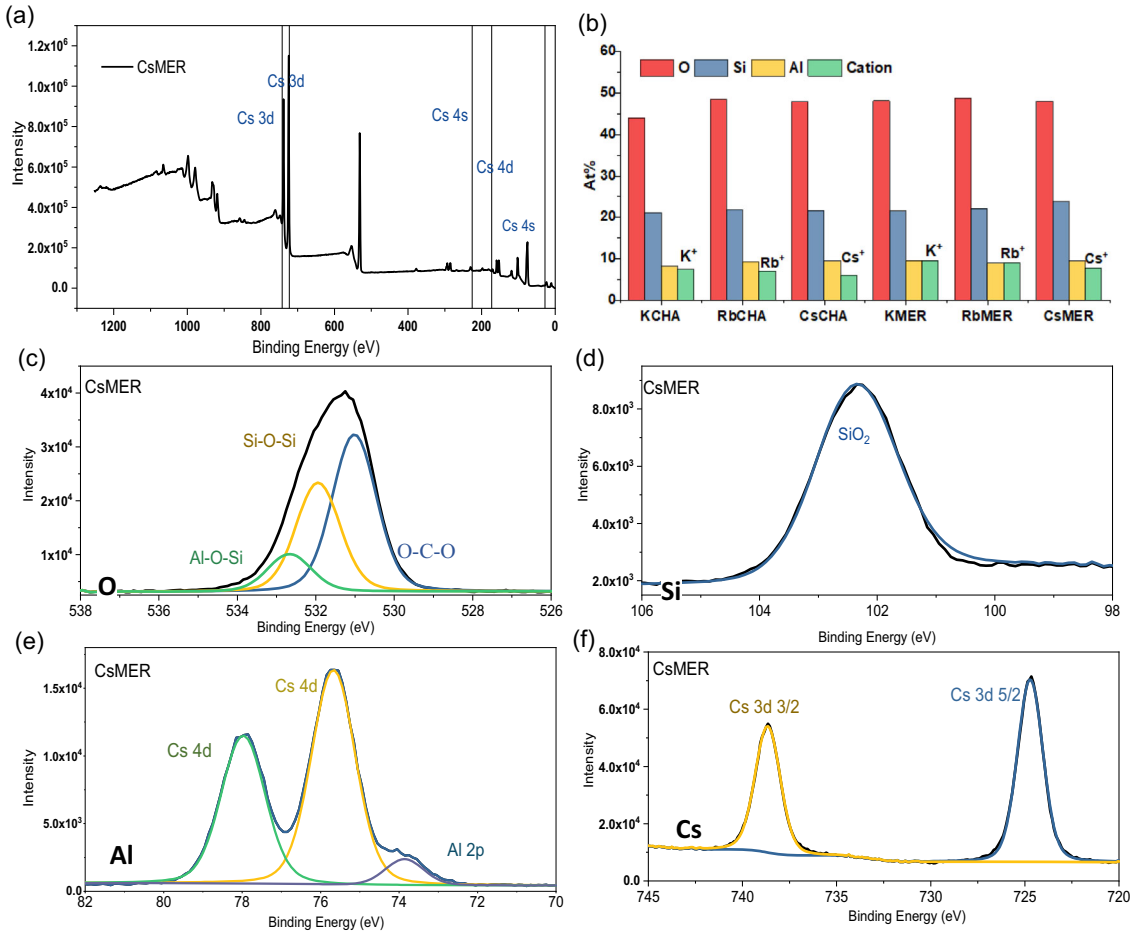

Figure 2. a) Full XPS spectrum of CsMER. b) Elemental distribution (in atomic %) of O, Si, Al, and functional cations in KCHA, RbCHA, CsCHA, KMER, RbMER, and CsMER. c) Experimental and fitted characteristic peaks of O in CsMER. d) Experimental and fitted characteristic peaks of Si in CsMER. e) Experimental and fitted characteristic peaks of Al in CsMER with a detailed view of the Al 2p peak. f) Experimental and fitted characteristic peaks of Cs in CsMER.

Figure S2–S7, Supporting Information). Frameworks with K^+ exhibited the lowest O atomic% (at%) and the highest Si at%. A comparative analysis of cation exchange efficiency revealed that cations in CHA exhibited lower atomic percentages compared to MER frameworks with K^+ suggested 7.40% in CHA but 9.60% in MER; Rb^+ weight 7.05% in CHA and 9.13% in MER; and Cs^+ only took 6.03% in CHA but 9.20% in MER. These results indicate that MER frameworks demonstrate a better cation exchange capability under identical alkaline conditions, achieving greater displacement of the native cations within the zeolite structures compared to CHA frameworks. XPS analysis of CHA and MER frameworks were subjected to similar cation exchange protocols (details in Figure S2–S6, Supporting Information), indicating an identical chemical bonding environment across both framework types. In all synthesized frameworks, characteristic spectral signatures corresponding to Al, Si, and O framework constituents were uniformly detected, validating the presence of essential chemical bonding configurations requisite for the formation of archetypal MER and CHA zeolite frameworks.

Three distinct types of oxygen bonding contributed to the O 1s peak (530.90 eV):[42] Si–O–Si (≈531.94 eV),[43,44] Al–O–Si (≈532.67 eV),[45] and O–C–O (≈531.01 eV) (Figure S3, Supporting Information),[46–48] indicating that the structural framework was predominantly composed of SiO_2 structure, complemented by Al_2O_3 structure. The appearance of carbon–oxygen bonds stemmed from the use of carbon as a calibration standard during surface analysis, producing an additional peak. The presence of the extra carbon peaks was also noticed at the representative binding energy that corresponded to C–C (≈284.48 eV), CO (≈284.82 eV), and CO_2 (≈288.27 eV) (Figure S4, Supporting Information).[46] The Si 2p peak, observed at 102.20 eV, confirmed that O-Si–O, the fundamental building block of the framework's cage-like structure, was the sole silicon chemical state present (Figure S5, Supporting Information).[49,50]

The characteristic Al 2p peak overlaps with the Cs 4 d response in frameworks with Cs^+ incorporated frameworks. Nevertheless, composite Al peaks remained consistent across all samples, with a prominent peak at 74.04 eV[51] (assigned to Al_2O_3, associated with bonds connecting 8MRs and 6MRs), aligning with the O 1s peak fitting results (Figure S6, Supporting Information).[52,53] The presence of specific functional cations was confirmed in all tested samples (Figure S7, Supporting Information). For the same cation, the chemical state generated on the MER and CHA framework was identical, implying that these cations occupied analogous positions within both structures. Additionally, atomic weight percentages derived from XPS, as shown in Figure 2b, confirm closely aligned Si/Al ratios (2.40 ± 0.15) across all samples, minimizing the influence caused by the difference in elemental contribution in frameworks.

Detailed bonding environments were further elucidated by Fourier transform infrared spectroscopy (FTIR, **Figure 3**a,b, more detail in Figure S8 and S9, Supporting Information), complementing the XPS data. The presence of H_2O (as crystal water) was confirmed between 3600 cm^{-1} and 3200 cm^{-1}, and O–H stretching within the frameworks was observed around 1600 cm^{-1}.[24,54] Characteristic peaks specific to the frameworks were primarily below 1100 cm^{-1}, where the difference between CHA and MER frameworks can be observed. Noticeably, the characteristic peaks of both frameworks shifted to the lower wavenumber area with heavier exchanged cations in the framework, indicating that these characteristic peaks are energetically sensitive to the metal cations, and suggesting the energy required for the cations to be displaced may be different.

Notably, strong transmission peaks around 1000 cm^{-1} were observed, corresponding to asymmetric Si–O stretching vibrations[55,56] or SiO_4 tetrahedral stretching vibrations in frameworks.[28,57] Significant spectral differences between all MER and CHA frameworks can be noticed, mostly caused by the basic unit formed at the beginning of the zeolite synthesis (Figure 3a), including symmetric Si–O–Si stretching in four-member rings (4MR, 790–720 cm^{-1}),[58,59] six-membered rings vibration (6MRs, 650–600 cm^{-1}),[60] stretching of double six-member rings (D6Rs) (around 520–460 cm^{-1}),[37,61] and the internal vibrations of Si–O and Al–O tetrahedra (462–410 cm^{-1}).[62,63] Since the 8MRs and cages are formed by the connection of 4MRs and 6MRs,[64] variations in these smaller units lead to structural differences in the 8MRs (the trapdoor structure, as shown in Figure 1) and may result in differences in gas sorption properties between the two types of frameworks. The local environment of Si in the framework is influenced by the number of nearby Al atoms (0, 1, 2, 3, or 4),[65] leading to asymmetric Si–O–Si and Si–O–Al stretching, indicative of a nonuniform Al environment. This asymmetric peak fitting in both MER and CHA frameworks (Figure 3b) confirmed that the frameworks exhibit three different types of asymmetric stretching when the pores are blocked by the cations.

2.2. Critical Temperature Measurements

From previous studies,[18] gases like H_2 rely on extra thermal energy input to diffuse through the 8MRs, and the minimum temperature required to provide sufficient thermal energy is known as the critical temperature (T_c). The critical temperatures of all materials were determined to estimate the optimal temperature ranges for hydrogen and deuterium separation at 1 bar (**Figure 4**).

The influence of the trapdoor cations on the critical temperature was observed in both frameworks. CHA and MER containing K^+ cations did not show an increasing trend in H_2 uptake in the measured temperature range (290 K to 360 K), indicating that the T_c of H_2 in both frameworks is lower than the temperatures tested, consistent with the T_c recorded for N_2 on KCHA (266 K).[23] As the size of the trapdoor cations in the frameworks increased (K^+ ($r = 1.52$ Å)[66] < Rb^+ ($r = 1.66$ Å)[67] < Cs^+ ($r = 1.81$ Å)[68]), the T_c for H_2 also increased (333 K for RbCHA, 343 K for CsCHA; 338 K for RbMER, 345 K for CsMER), suggesting that frameworks with heavier trapdoor cations require more thermal energy for H_2 to traverse the functional windows.

Elevating the temperature from 310 K to 358 K enhanced H_2 adsorption in both Rb and Cs-exchanged frameworks, attributable to increased thermal energy facilitating molecular diffusion. The Rb exchanged CHA framework exhibited the highest H_2 uptake, suggesting incomplete occlusion of trapdoor apertures by Rb^+ cations, thereby enabling unrestricted guest molecule access. Conversely, Cs-exchanged MER frameworks demonstrated higher H_2 adsorption capacities compared to Rb-exchanged MER variants,

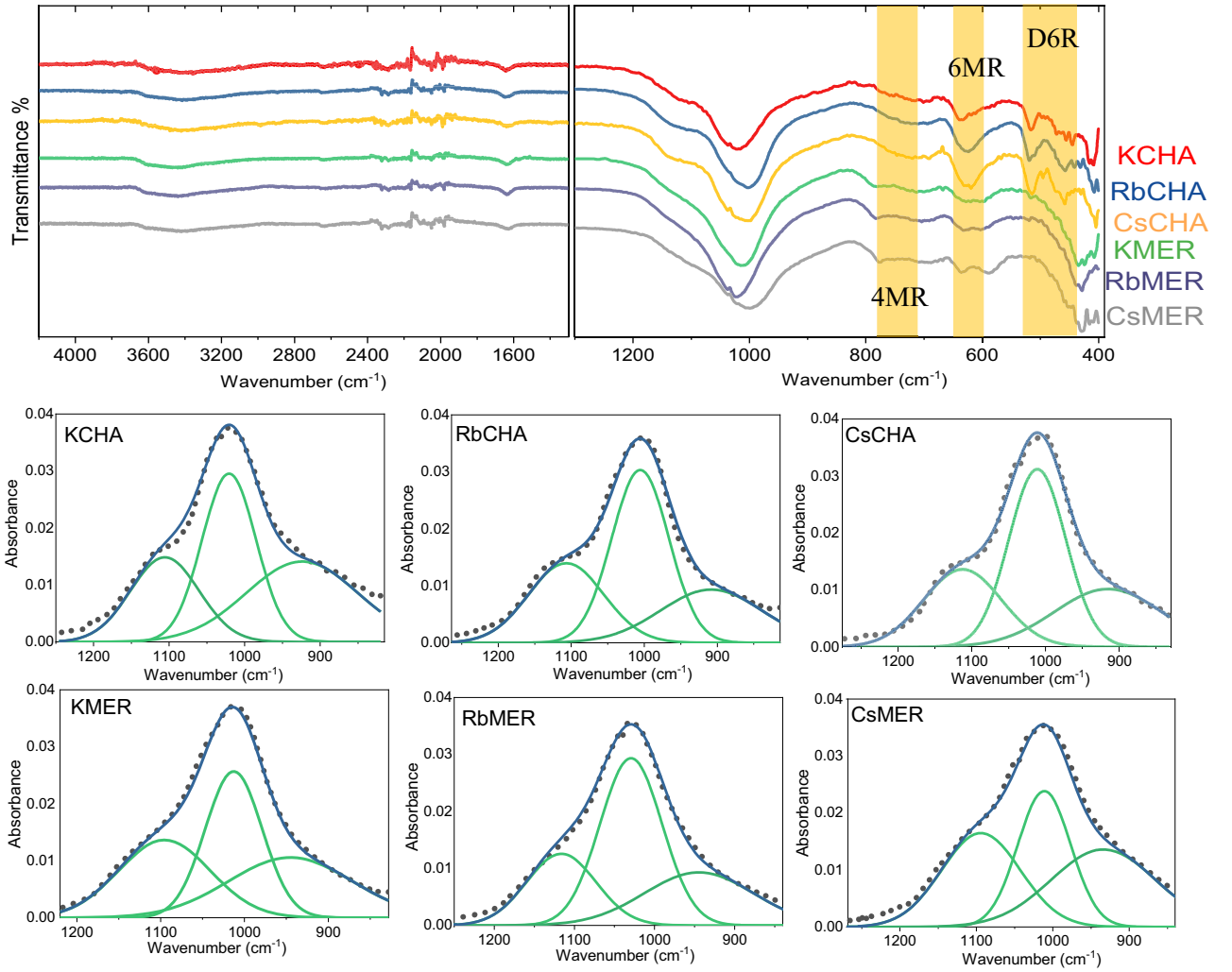

Figure 3. a) Full range IR spectra ranging from 4500 cm^{-1} to 400 cm^{-1} for KCHA (red), RbCHA (blue), CsCHA (yellow), KMER (green), RbMER (purple), and CsMER (gray). b) Experimental data points (black dots) between 1250 cm^{-1} and 850 cm^{-1} fitted with a curve (navy) derived from three individual peaks (green).

highlighting framework-specific cation effects on pore accessibility. Since the thermal effect primarily influences functional windows blocked by the alkali metal cation,[18,23] more cations sitting on the trapdoor windows can cause a distinct response in thermal energy variation. The increased H_2 adsorption capacity observed in CsMER relative to RbMER at temperatures approaching the critical threshold may imply that CsMER exhibits a greater number of accessible diffusion pathways. This observation indicates that a higher proportion of Cs^+ cations are displaced from the center of the thermally controlled windows (8MRs) compared to Rb^+ cations. In other words, Cs^+ are more likely to sit in the trapdoor windows in the MER framework compared to Rb^+ cations. This positioning could lead to a more pronounced increase in sorption as the temperature approaches and surpasses the critical temperature, thereby opening functional windows. These observations are consistent with XPS results, which showed a higher atomic percentage of Cs^+ compared to Rb^+ in both MER and CHA frameworks. When the temperature exceeds the threshold for H_2, the H_2 molecules can be adsorbed on the internal pore volume guarded by the trapdoor (8MR) sites that are typically blocked by the cation at lower temperatures.

To further explore the structural influence of the adsorbed hydrogen isotopes on trapdoor frameworks, neutron diffraction measurements of zeolite frameworks under H_2 and D_2 at different thermal conditions were conducted. However, due to the limited adsorption amount at temperatures above room temperature, the information generated from the neutron diffraction was limited (Figure S11–S19, Supporting Information). In trapdoor zeolites, the sorption of both H_2 and D_2 occurs via physical adsorption, resulting in nearly identical neutron diffraction patterns across all tested temperatures (Figure S11, Supporting Information). The distinction between physical sorption and thermal effects was highlighted by comparing diffraction patterns at 345 K with baseline measurements at 300 K. For H_2, elevated temperatures caused an upward shift in the diffraction background, which persisted even after cooling to 300 K (the baseline temperature) with 1 bar H_2 dosed (Figure S12–S13, Supporting Information). In contrast, for D_2, shifts observed under similar thermal conditions

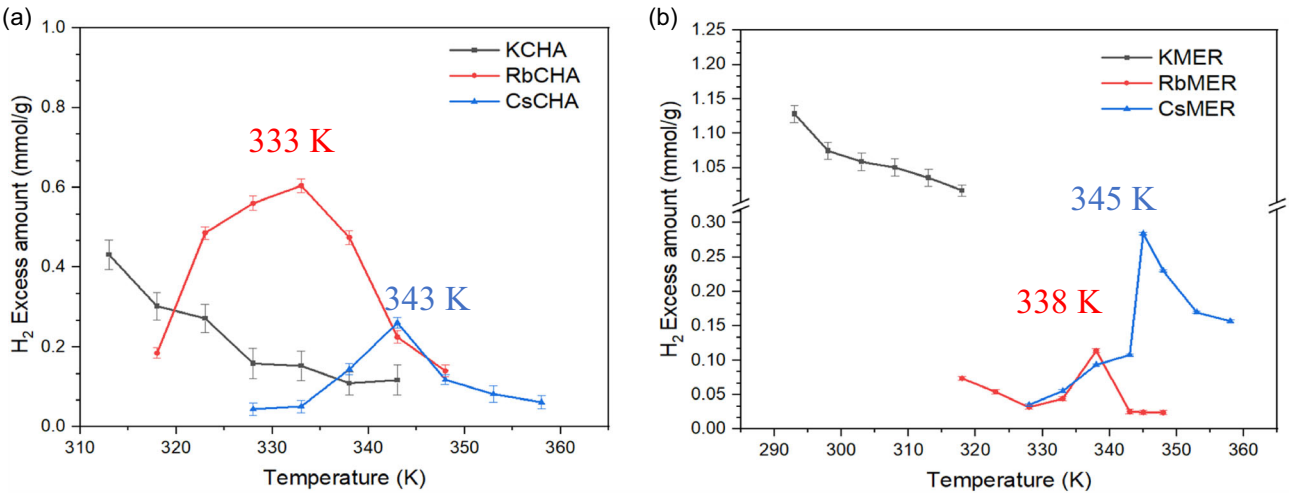

Figure 4. Measured hydrogen uptakes at variable temperatures at 1000 mbar on a) CHA frameworks (K^+ in black, Rb^+ in red, and Cs^+ in blue). b) MER frameworks (K^+ in black, Rb^+ in red, and Cs^+ in blue). Critical temperatures are indicated.

appeared primarily linked to thermal effects (Figure S14 and S15, Supporting Information). Upon cooling back to 300 K, the neutron diffraction patterns of D_2 dosed samples closely aligned with the baseline on all test samples, which suggests that the adsorption of D_2 was not blocked by cations at the measured temperatures (Figure S16–S19, Supporting Information). However, this discrepancy between observations with H_2 and with D_2 may stem from D_2's smaller neutron cross section, which reduces its detectability in neutron diffraction, potentially masking adsorption within the trapdoor-guarded pore volume. Consequently, additional sorption studies are necessary to fully elucidate these interactions.

2.3. Low-Pressure H_2 and D_2 Sorption

Critical temperature measurements indicated that H_2 can benefit from increased extra thermal energy input from room temperature up to critical temperature (Figure 4). To achieve the best separation of H_2 and D_2 within these frameworks, the selected temperature should ensure the maximum adsorption difference between D_2 and H_2. Thus, the selected operation temperature should be significantly below the recorded T_c (333 K on RbCHA; 343 K on CsCHA; 338 K on RbMER; 345 K on CsMER) for H_2.

The detailed surface areas and pore size distributions of the CHA and MER zeolites used in this study have been previously reported,[18] where both frameworks were confirmed to exhibit microporosity consistent with typical trapdoor zeolites. The earlier study also demonstrated that larger exchanged cations within the frameworks led to reduced surface area and a broader pore size distribution. The higher surface area of CHA frameworks versus MER frameworks was reflected in the greater sorption quantities in both H_2 and D_2 (**Figure 5**a,b). In general, D_2 was preferred by both framework structure types compared to H_2 at 77 K, and the preference existed for all three cation-exchanged porous systems. Compared to other materials, KCHA, with the smallest cation size (radius r = 1.52 Å) and the more porous CHA framework, exhibited the highest sorption amount in both H_2 and D_2 at

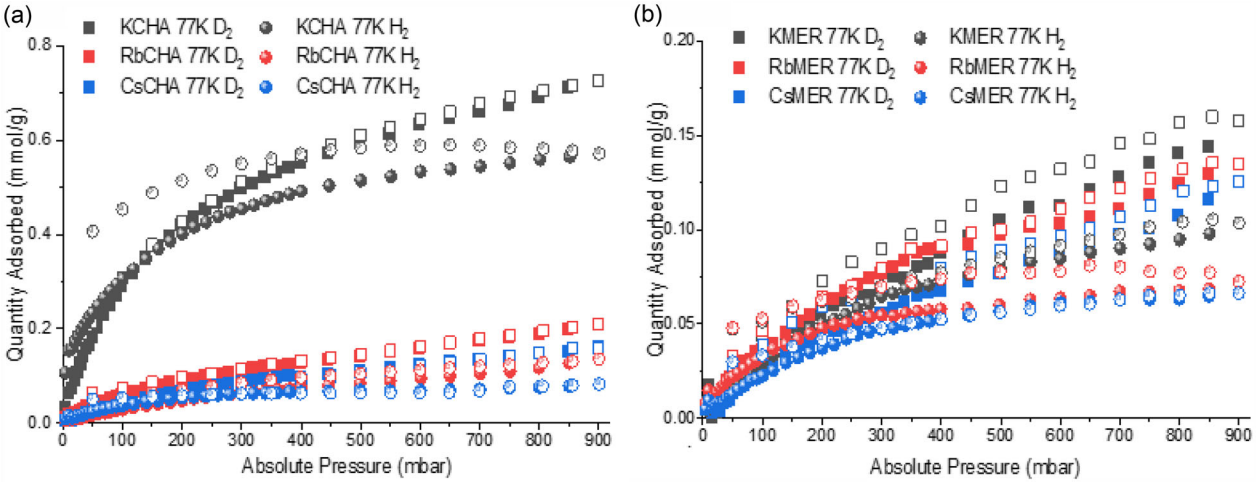

Figure 5. Adsorption (solid symbols) and desorption (empty symbols) of H_2 (represented by spheres) and D_2 (represented by squares) on a) KCHA (black), RbCHA (red), and CsCHA (blue) at 77 K. b) KMER (black), RbMER (red), and CsMER (blue) at 77 K.

77 K (**Table 1**). However, the quantitative difference between the amount of H_2 and D_2 adsorbed on KCHA is the lowest, suggesting that the difference in accessible capacity between H_2 and D_2 in the KCHA framework is lower than in heavier cation-exchanged frameworks.

The diminished efficacy of separation of K^+ in CHA frameworks is likely to arise from steric incompatibility, as K^+ (ionic radius ≈ 1.52 Å) provides suboptimal occlusion of 8MRs (functional radius $r = 1.9$ Å), thereby negating the trapdoor mechanism's capacity for discriminative H_2/D_2 separation at 77 K. In contrast, the MER frameworks exhibit anisotropic 8MR pore architectures with reduced dimensions ($r = 1.05$ Å, 1.13 Å, and 1.80 Å), enabling K^+ to achieve near-complete steric hindrance across two orthogonal pore orientations, thus preserving selective molecular sieving functionality. The enhanced efficacy of the trapdoor mechanism under these conditions amplifies the differential adsorption capacities of H_2 and D_2, yielding a 14% increase in the D_2/H_2 selectivity ratio relative to KCHA (Table 1). This trend, wherein heavier exchanged cations correlate with progressively higher D_2/H_2 adsorption ratios, underscores the heightened propensity of D_2 to lower the energy barrier of the door-keeping cation and diffuse through the gate at elevated temperatures.

For both types of frameworks, upon increasing the cation size ($K^+ < Rb^+ < Cs^+$), the ratio of adsorbed D_2 to adsorbed H_2 increases at 77 K, with the highest ratio observed in Cs^+ containing frameworks (1.894 in CsMER). Although the increase in cation size limited the adsorption of guest molecules by blocking the pores, the quantitative difference (in the percentage) of adsorbed H_2 and D_2 increased with cation size, which indicates that the cation size directly influences the blockage of the functional windows (8MRs) and determines the adsorption difference between H_2 and D_2, indicating the potential of separating H_2 and D_2 with trapdoor systems.

Table 1. H_2 and D_2 sorption results of all samples at 900 mbar and 77 K.

	KCHA	RbCHA	CsCHA	KMER	RbMER	CsMER
Amount of adsorbed D_2 at 900 mbar 77 K [mmol g^{-1}]	0.719	0.209	0.159	0.158	0.135	0.125
Amount of adsorbed H_2 at 900 mbar 77 K [mmol g^{-1}]	0.570	0.145	0.085	0.103	0.072	0.066
D_2/H_2	1.261	1.441	1.869	1.600	1.876	1.894

2.4. Kinetic Analysis

To gain a more profound understanding of the H_2 and D_2 diffusion processes within the frameworks, we calculated the mass transfer coefficient (k) (see **Figure 6**, with calculations based on Equation (1) and (2)) for the adsorption process of H_2 and D_2 at 77 K. The times required for the complete D_2 adsorption process at 77 K were uniform across all cation-exchanged CHA and MER frameworks (Figure S20, Supporting Information), demonstrating that D_2 molecules can diffuse through the pores freely in all the frameworks without blockage of the trapdoor windows at temperatures below the threshold temperature.

On the contrary, the time required for the entire adsorption process for H_2 at 77 K increased slightly in Rb^+ and Cs^+ exchanged frameworks compared to K^+ exchanged frameworks, suggesting some hindrance encountered by H_2 molecules during diffusion through the windows blocked by the alkali metal cations and necessitating prolonged periods in navigating accessible diffusion pathways. During the adsorption process within a lower pressure range (<100 mbar), a stage where the guest molecules are spontaneously adsorbed on the porous surface, the equilibration time for D_2 was longer than for H_2 (refer to Figure S20–S26, Supporting Information). This indicated the potential existence of more diffusion pathways available for D_2 which induced longer equilibration times in the pores and led to higher sorption amounts.

Across all the synthesized frameworks, the mass transfer coefficient (k) exhibited a monotonic pressure-dependent increase at 77 K for both H_2 and D_2 adsorbates (Figure 6). Adsorption isotherms for both isotopes adhered to a quasilinear progression within the studied pressure regime. The fluctuation in the k results observed in MERs could likely be attributed to the limited

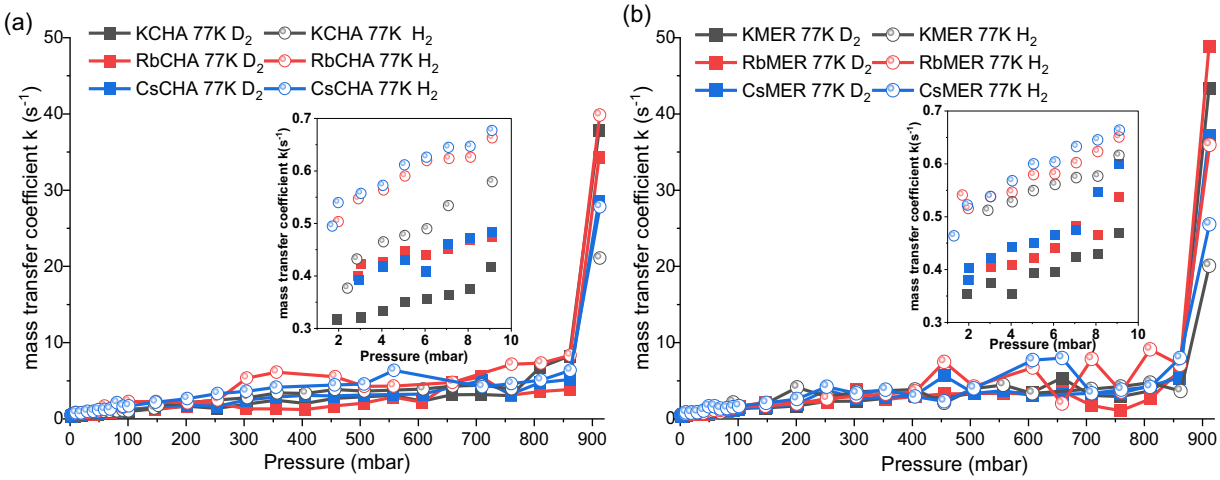

Figure 6. Mass transfer coefficient k (s^{-1}) for H_2 (solid squares) and D_2 (open spheres) at 77 K in a) KCHA (black), RbCHA (red), and CsCHA (blue) with detailed plot up to 10 mbar (inset). b) KMER (black), RbMER (red), and CsMER (blue) with detailed plot up to 10 mbar (inset).

accessible porosities of the frameworks. The accessible microporous volumes reached capacity at ≈400 mbar, prompting subsequent diffusion of the guest molecules alongside the external surface upon further pressure increase. The uptake rate for D_2 was slower across all samples at the same pressure until 900 mbar when the adsorption process concluded, compared to the H_2 results. This difference becomes more pronounced when focusing on the lower pressure range (<10 mbar). Frameworks containing K^+ displayed the lowest k values in both CHA and MER structures, indicating slower uptake kinetics in KCHA and KMER than in heavier cation (Rb^+ and Cs^+) containing frameworks. This trend implies that heavier cations (Rb^+, Cs^+) facilitate higher kinetic rates at equivalent pressures, likely due to steric effects that restrict pore accessibility, thereby accelerating equilibration by limiting diffusion pathways with faster equilibrium at the same pressure. The KCHA framework, specifically, showed a significantly lower mass transfer coefficient (k) for both D_2 and H_2 (0.2 s^{-1} lower for H_2 and 0.1 s^{-1} lower for D_2 when compared with RbCHA and CsCHA). Considering the highest adsorption results were obtained for both D_2 and H_2 from KCHA, it is plausible that the slower kinetic rate is due to the presence of higher porosities for the guest molecules within KCHA, as K^+ cannot fully block the 8MRs in the CHA framework. RbCHA had similar kinetic rates to CsCHA for both D_2 and H_2, albeit slightly slower. The same pattern was observed in MER frameworks, suggesting that the exchanged cation is the primary factor affecting kinetic behavior.

As pressure increased, gradual compression and crowding of guest molecules inside the pores caused adsorbed H_2 to move through the pores, which resulted in variability in the uptake steps and extended step durations after equilibrium. In contrast, the step duration for D_2 decreased with rising pressure, indicating that at higher pressure (>500 mbar), D_2 could penetrate the pores more easily than H_2 (Figure 6). These varied behaviors further indicate that H_2 and D_2 are likely to follow different pathways in the porous system, each possessing unique accessible capacities. The largest kinetic differences between H_2 and D_2 at 10 mbar and 100 mbar, in ratio terms, were provided by KMER, RbCHA and CsCHA (Table S1, Supporting Information). In MER frameworks, the mass transfer coefficient between H_2 and D_2 decreased with the inclusion of heavier cations. In contrast, in CHA frameworks, this difference increases with cation size, particularly at 100 mbar.

Equilibration time calculations (detailed in Equation (2), the time needed to reach adsorption equilibrium at each pressure step, t_e) further reinforced the kinetic results generated from the diffusion process (**Figure 7**). H_2 reached equilibrium faster than D_2 in both MER and CHA frameworks, with a shorter t_e at 77 K, consistent with the higher kinetic rate observed for H_2. Results generated on MER were more variable than on CHA as depicted by the mass transfer coefficient (Figure 6) and required a higher pressure to stabilize, indicating the framework's structure influenced the kinetics of the diffusion process. The exchanged cations did not noticeably affect the t_e of H_2 on CHA frameworks at pressures below 10 mbar. However, the K^+ confined MER frameworks exhibited a longer t_e compared to Rb^+ and Cs^+ exchanged MERs.

Above 250 mbar, the time H_2 took to reach equilibrium fell below 1 s on both frameworks. Still, at lower pressure (<50 mbar), MERs showed higher t_e values for H_2. This extended equilibrium time for MER below 250 mbar might be due to the availability of different pathways (accessible windows) with varying diameters compared to CHA frameworks. The minimum reading of t_e of H_2 on the instrument was achieved at around 550 mbar on all candidates, indicating the pores had been fully occupied by the guest molecules at that pressure. By comparison, this value for D_2 was not reached until 600 mbar on CsCHA or 700 mbar on RbMER, further confirming that more surfaces and pathways are accessible to D_2 in these frameworks than for H_2. In contrast to H_2, the time required for full D_2 adsorption exhibited a clear influence from the trapdoor cations: KCHA exhibited the longest t_e below 250 mbar compared to RbCHA and CsCHA; correspondingly, CsMER had the shortest t_e below 250 mbar compared to RbMER and KMER.

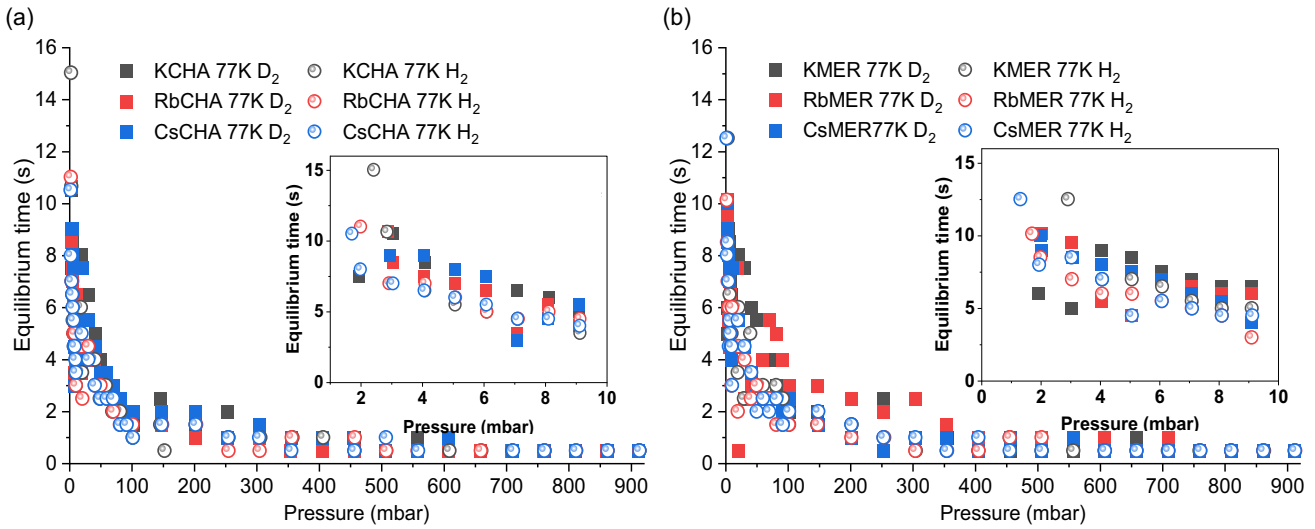

Figure 7. Equilibration time (s) for H_2 (solid square) and D_2 (open sphere) at 77 K in a) KCHA (black), RbCHA (red), and CsCHA (blue) with detailed plot up to 10 mbar. b) KMER (black), RbMER (red), and CsMER (blue) with detailed plot up to 10 mbar.

The inverse relationship between cation size and equilibrium time shows that reduced porosities due to larger cation size can result in faster D_2 equilibrium. Additionally, the impact of the exchanged cation on the framework seems to be more pronounced in D_2 sorption experiments, suggesting that some pathways (windows) containing the trapdoor cations, such as the 8MRs, are exclusively accessible to D_2. The shortest t_e on CsMER can also be attributed to the reduced porosities as the cation not only sits on the functional windows.[69] Trapdoor zeolites, as studied here, offer a unique approach by employing kinetic selectivity via dynamic cation gating at liquid nitrogen temperature (77 K). This approach balances practicality and performance by harnessing differences in diffusion behavior rather than solely equilibrium adsorption selectivity. To provide context, **Table 2** summarizes reported selectivity values, operating temperatures, and mechanisms for representative materials used in hydrogen isotope separation:

This comparison highlights that while trapdoor zeolites may not achieve the highest absolute selectivities, their operating conditions are more accessible and scalable, making them promising candidates for practical hydrogen isotope separation technologies. The kinetic differences observed here between H_2 and D_2 in the trapdoor system can be used to inform methods of for separating these hydrogen isotopes using a breakthrough system. With a shorter equilibrium time and a lower sorption amount, H_2 would pass through an absorbent bed of the trapdoor zeolite more quickly than any D_2 present, and higher purity H_2 stream could be collected first after the breakthrough process. The separation results of the hydrogen isotopes can be benefited by extending the length of the breakthrough bed and increasing the difference in diffusion time of the hydrogen isotopes. Since the sorption process is fully reversible, the guest isotopes remaining in the bed can be removed easily by pressure swing.

While the current work focuses on single-component H_2 and D_2 sorption at cryogenic conditions, future studies will explore their separation behavior in mixed-gas systems under elevated temperatures. Prior reports suggest some level of D_2 selectivity in trapdoor zeolites like CsCHA at ambient temperature;[70] however, the extent to which kinetic differences can be exploited across temperature ranges remains an open question. Mixed-gas adsorption and breakthrough experiments will be essential to fully assess the practical potential of these materials for isotope separation under more realistic conditions.

Table 2. Summary of different types of porous materials applied in hydrogen isotope separation.

Material type	Operating temperature	Mechanism	Quantitative selectivity (D_2/H_2)	Reference
Palladium alloys	>300 °C	Chemical affinity	High (variable)	[9,78]
MOFs	≤77 K, maximized at 30 K	Chemical affinity quantum sieving	Up to 10–20	[79,80]
POCs and COFs and small pore zeolites	≤77 K maximized at 30 K	Kinetic quantum sieving	Moderate	[14,33,81]
Trapdoor zeolites	77 K	Kinetic trapdoor selectivity	≈1.9 (900 mbar)	This study

3. Conclusion

This study aimed to demonstrate the possibility of applying a trapdoor system in hydrogen isotope separation by exploring the influence of the trapdoor structure and exchanged cations in both thermal and kinetic responses. Structural distinctions between CHA and MER frameworks were confirmed through XPS and FTIR analyses, revealing that variations in symmetric bonding configurations define their unique architectures and porosity profiles, despite both exhibiting functional trapdoor mechanisms. Isobaric sorption measurements experimentally validated the presence of a threshold temperature for H_2 diffusion, confirming the trapdoor effect. The critical temperature of the frameworks was shown to be dependent on the mass of the trapdoor cations ($T_{Cs^+} > T_{Rb^+} > T_{K^+}$).

A preference for D_2 over H_2 can be seen from the gas sorption, as evidenced by higher sorption quantities and faster equilibration times. The isothermal gas sorption confirmed the Cs^+ cations resulted in the highest D_2/H_2 uptake ratio generated on 900 mbar at around 1.9, probably due to the best blockage of the functional window, maximizing the opening and closing behavior of the trapdoor. However, the larger cation size also limited the adsorption ability of the frameworks. CHA frameworks with higher framework porosities can cooperate better with heavier cations than MER.

Both isothermal and kinetic results demonstrate that D_2 has a higher likelihood of penetrating the cation-blocked functional windows (8MRs) compared to H_2 at temperatures below the critical temperature. This results in a slower diffusion rate for D_2, with observable saturation occurring at lower pressures when pores remain unoccupied by adsorbates. Furthermore, the kinetic dynamics of hydrogen isotopes are significantly governed by the identity of exchanged cations within the frameworks. Considering the straightforward synthesis of CHA and MER frameworks from commercial Y-zeolites, this approach holds strong promise for scalable industrial applications requiring efficient hydrogen isotope separation. Moreover, given the demonstrated thermal and radiation stability of these frameworks,[18] the trapdoor mechanism may be extended to the separation of tritium (T_2) from hydrogen at cryogenic temperatures, with further studies needed to evaluate its selectivity.

In conclusion, KMER and RbCHA emerge as the materials best suited for hydrogen isotope separation at 77 K below 500 mbar owing to their pronounced kinetic contrast and quantitative differentiation between H_2 and D_2, alongside practical adsorption capacities. These findings underscore that zeolites with trapdoor mechanisms could represent viable options for efficient H_2/D_2 separation under cryogenic conditions.

4. Experimental Section

Synthesis of Zeolites: The synthesis of CHA and MER zeolites was performed following the method established by Kim et al.,[71] and the ion exchange process was conducted in accordance with previously established research.[18] The synthesized samples were dried in open air for over 72 h at room temperature.

Structural characterization of the CHA and MER zeolite frameworks (including energy-dispersive X-ray spectroscopy, powder X-ray diffraction, and simultaneous thermal analysis) has been reported in detail in our previous work.[18] Representative SEM images of the CHA and MER samples are provided in the Supplementary Information.

XPS: The XPS experiments were carried out to confirm the presence of specific inorganic groups. These experiments were performed using a Kratos Axis SUPRA XPS system equipped with an Al Kα X-ray source with monochromatic light (1486.7 eV), a spherical sector analyzer, and three multichannel resistive plates as well as 128 channel delay line detectors. The experiments were conducted at 150 W power with a spot size of 700×300 μm. Survey scans were performed at a pass energy of 160 eV, and more detailed scans at a pass energy of 20 eV. Electron charge neutralization was accomplished using a magnetic immersion lens. The experiment parameters included a filament current of 0.27 A, a charge balance of 3.3 V, and a filament bias of 3.8 V. All experimental data were gathered under a pressure below 10^{-8} Torr and at a room temperature of 294 K on the powder samples. Data were analyzed with CasaXPS v2.3.20PR1.0 software, and the spectra were calibrated with the C1s peak at 284.8 eV.

FT-IR: A mid-infrared attenuated total reflectance spectrometer (Spectrum Two by Perkin-Elmer, USA) was utilized to identify the characteristic bonds in the zeolites. We examined powdered samples under atmospheric conditions and at room temperature, using both transmission and absorption modes. Analysis of the spectral data was conducted using PerkinElmer Spectrum, a proprietary software offered by the spectrometer's manufacturer.

Critical Temperature Measurement: The critical temperatures of H_2 for all materials were ascertained using a Hiden Isochema XEMIS gravimetric sorption instrument. These measurements were conducted isothermally at various temperatures, ranging from 303 K to 360 K, utilizing a water bath for temperature control. The pressure was manipulated from 0 to 5 bar with a buoyancy correction applied based on a helium measurement at room temperature. All gases used for these experiments were supplied by BOC with a purity of 99.999%. To remove moisture, the powder samples (around 80 mg) were degassed under a high vacuum (10^{-7} mbar) at 473 K for over eight hours prior to the measurements.

Gas Sorption and Kinetic Analysis: Gas sorption measurements were performed on a Micromeritics 3-Flex instrument in the range of 0 to 1 bar at two different temperatures: 77 K (controlled by liquid N_2) and 273 K (ice bath). The gases utilized in the experiment, namely H_2 (99.999%) and D_2 (99.999%), were supplied by BOC. Comprehensive degassing was ensured by exposing the samples to a high vacuum (10^{-7} mbar) at 473 K for over 8 h before the measurements. Low-pressure sorption kinetics of H_2 and D_2 were collected on the 3-Flex and analyzed via MATLAB for step fitting and equilibrium time calculation.

Kinetic quantum sieving of hydrogen isotopes was effectively ruled out in the cation-exchanged frameworks at the experimental conditions, as the cation exchange processes obstructed the aperture sizes required to induce the quantum effect.

Kinetic analyses for H_2 and D_2 sorption were performed utilizing the linear driving force (LDF) model.[72,73] LDF, a modified version of the general diffusion equation (Fickian diffusion),[74] is suited for isothermal adsorption analysis of pure guest molecules in a single porous adsorbent.[75] In this model, the kinetic coefficient can be derived from the adsorbent fractional uptake of each step. The fractional uptake at the measured time[76] (θ_t) of each step is calculated as per Equation (1)

$$\theta_t = (n_t - n_0)/(n_\infty - n_0) \quad (1)$$

where n_0 is the adsorbed volume at the beginning of the adsorption step and n_t, and n_∞ represents the adsorbed volume during equilibration and at equilibrium, respectively. The fractional uptake can also be described as a function of time and mass transfer coefficient k[77] as shown in Equation (2)

$$\theta_t = \frac{V_{it}}{V_{i\infty}} = k(n_\infty - n_t) = n_0 + (n_\infty - n_0)\,[1 - \exp(-k(t - t_0))] \quad (2)$$

where V_{it} is the uptake volume of the gas at time t, t_0 is the time at the start of the pressure step, n_t is the adsorbed volume at time t, $V_{i\infty}$ is the uptake volume at the equilibrium of the measured pressure step, and n_∞ is the amount absorbed at equilibrium. Therefore, under isothermal conditions for a pure gas input, $V_{it}/V_{i\infty}$ is referred to as the adsorbent fractional uptake (θ_t) for the measured pressure, and k can be viewed as the kinetic rate constant. The equilibrium time (t_e) is defined as the time required for 95% of the guest molecules to have been adsorbed at the recorded pressure step.

SEM: SEM images were captured at 15 kV and a working distance of 10 mm with an IT300 SEM instrument from JEOL, Japan. After mounting the samples onto a conductive carbon tape, they were coated with a thin layer of high-purity graphite (10−15 nm), using a Q150TES coater from Quorum Technologies Ltd., UK, to prevent electron charging and optimize characteristic X-ray collection.

Acknowledgements

The authors are grateful for the beamtime offered by STFC Rutherford Appleton Laboratory (RB2310530), Ivan da Silva for assistance with the neutron diffraction experiment and funding support from EPSRC (Ref: EP/Y007778/1).

Conflict of Interest

The authors declare no conflict of interest.

Author Contributions

Dankun Yang: synthesis; methodology; data analysis; and writing of the manuscript. **Huan V. Doan**: conceptualization; supervision and review and editing of the manuscript. **Sebastien Rochat**: Supervision and review and editing of the manuscript. **Ivan da Silva**: helped in GEM data collection and review. **Thomas B. Scott**: funding acquisition; supervision; and review. **Valeska P. Ting**: conceptualization; funding acquisition; supervision; and review and editing of the manuscript. **Shaoliang Guan**: assistance with XPS measurements. **Mi Tian**: review and editing of the manuscript. All authors have read and agreed to the published version of the manuscript.

Data Availability Statement

The data that support the findings of this study are available from the corresponding author upon reasonable request.

Keywords

gas sorption, hydrogen isotope separation, kinetic analysis, nanoporous zeolites, trapdoor behavior

Received: April 4, 2025
Revised: June 2, 2025
Published online:

[1] R. K. Sinha, S. K. Sinha, K. B. Dixit, A. K. Chakrabarty, D. K. Jain, *Underst. Mitigating Ageing Nucl. Power Plants*, (Ed: P.G. Tipping), Woodhead Publishing, Oxford **2010**, pp. 732–794.
[2] A. I. Miller, *Can. Nucl. Soc. Bull.* **2001**, *22*, 1.
[3] S. Zheng, D. B. King, L. Garzotti, E. Surrey, T. N. Todd, *Fusion Eng. Des.* **2016**, *103*, 13.
[4] W. M. Rutherford, *Mater. Sci. Forum* **1988**, *31*, 19.
[5] *DOE Handbook: Tritium Handling and Safe Storage*, U.S. Department of Energy, Washington, DC **2007**, https://www.standards.doe.gov/standards-documents/1100/1129-bhdbk-2007.

[6] J. R. Alcántara-Avila, F. I. Gómez-Castro, J. Gabriel Segovia-Hernández, K. I. Sotowa, T. Horikawa, *Comput. Aided Chem. Eng.* **2014**, *33*, 1501.
[7] T. V. Vasyanina, I. A. Alekseev, S. D. Bondarenko, O. A. Fedorchenko, K. A. Konoplev, E. A. Arkhipov, V. V. Uborsky, *Fusion Eng. Des. J.*, **2008**, *83*, 1451.
[8] G. Chisholm, T. Zhao, L. Cronin, in *Storing Energy*, Elsevier, Great Britain **2022**, pp. 559.
[9] L. N. Baloyi, B. C. North, H. W. Langmi, B. J. Bladergroen, T. V. Ojumu, *South African J. Chem. Eng.* **2016**, *22*, 44.
[10] M. El-Shafie, *Int. J. Energy Res.* **2022**, *46*, 3572.
[11] D. Cao, H. Huang, Y. Lan, X. Chen, Q. Yang, D. Liu, Y. Gong, C. Xiao, C. Zhong, S. Peng, *J. Mater. Chem. A* **2018**, *6*, 19954.
[12] H. Oh, I. Savchenko, A. Mavrandonakis, T. Heine, M. Hirscher, *ACS Nano* **2014**, *8*, 761.
[13] K. Geng, T. He, R. Liu, S. Dalapati, K. T. Tan, Z. Li, S. Tao, Y. Gong, Q. Jiang, D. Jiang, *Chem. Rev.* **2020**, *120*, 8814.
[14] M. Liu, L. Zhang, M. A. Little, V. Kapil, M. Ceriotti, S. Yang, L. Ding, D. L. Holden, R. Balderas-Xicohténcatl, D. He, R. Clowes, S. Y. Chong, G. Schütz, L. Chen, M. Hirscher, A. I. Cooper, *Science* **2019**, *366*, 613.
[15] J. Y. Kim, H. Oh, H. R. Moon, *Adv. Mater.* **2019**, *31*, 1.
[16] J. M. Salazar, S. Lectez, C. Gauvin, M. Macaud, J. P. Bellat, G. Weber, I. Bezverkhyy, J. M. Simon, *Int. J. Hydrogen Energy* **2017**, *42*, 13099.
[17] S. H. So, H. Oh, *Int. J. Hydrogen Energy* **2024**, *50*, 539.
[18] D. Yang, H. V. Doan, U. O'Hara, D. Reed, J. Hungerford, J. Eloi, N. E. Pridmore, P. F. Henry, S. Rochat, M. Tian, V. P. Ting, *Langmuir* **2024**, *40*, 12394.
[19] J. J. Pluth, J. V. Smith, W. J. Mortier, *Mater. Res. Bull.* **1977**, *12*, 1001.
[20] N. Sobuś, I. Czekaj, V. Diichuk, I. M. Kobasa, *Tech. Trans.* **2020**, *43*, 1.
[21] P. A. Barrett, S. Valencia, M. A. Camblor, *J. Mater. Chem.* **1998**, *8*, 2263.
[22] O. D. F. M.D. Foster, I. Rivin b, M. M. J. Treacy, *Microporous Mesoporous Mater.* **2006**, *90*, 32.
[23] J. Shang, G. Li, R. Singh, Q. Gu, K. M. Nairn, T. J. Bastow, N. Medhekar, C. M. Doherty, A. J. Hill, J. Z. Liu, P. A. Webley, *J. Am. Chem. Soc.* **2012**, *134*, 19246.
[24] X. Zheng, Y. Li, W. Li, Z. Su, J. Xu, Y. Li, A. Yuan, Y. Xu, L. Zhai, *IOP Conf. Ser. Earth Environ. Sci.* **2020**, *453*, 012086, https://doi.org/10.1088/1755-1315/453/1/012086.
[25] J. Shang, G. Li, P. A. Webley, J. Z. Liu, *Comput. Mater. Sci.* **2016**, *122*, 307.
[26] F.-X. Coudert, D. Kohen, *Chem. Mater.* **2017**, *29*, 2724.
[27] T. Du, X. Fang, L. Liu, J. Shang, B. Zhang, Y. Wei, H. Gong, S. Rahman, E. F. May, P. A. Webley, G. Li, *Chem. Commun.* **2018**, *54*, 3134.
[28] X. Song, Y. Zhang, X. Cui, F. Liu, H. Zhao, *Adsorpt. Sci. Technol.* **2021**, *2021*, 1, https://journals.sagepub.com/doi/full/10.1155/2021/9994079.
[29] Á. Miguel, K. Quiroz-estrada, G. I. Hernandez-salgado, R. I. Portillo, J. Deisy, M. D. L. Á. Velasco, V. Petranovskii, *Separations* **2022**, *9*, 150.
[30] J. Shang, G. Li, R. Singh, P. Xiao, J. Z. Liu, P. A. Webley, *J. Phys. Chem. C* **2013**, *117*, 12841.
[31] M. Kong, Z. Liu, T. Vogt, Y. Lee, *Microporous Mesoporous Mater.* **2016**, *221*, 253.
[32] H. June, D. Jo, S. Bong, *Chem. Eng. J.* **2022**, *446*, 137100.
[33] R. Xiong, R. Balderas Xicohténcatl, L. Zhang, P. Li, Y. Yao, G. Sang, C. Chen, T. Tang, D. Luo, M. Hirscher, *Microporous Mesoporous Mater.* **2018**, *264*, 22.
[34] Y. Y. Milenko, L. V. Karnatsevich, V. S. Kogan, *Physica* **1972**, *60*, 90.
[35] D. G. Artiukhin, J. Kłos, E. J. Bieske, A. A. Buchachenko, *J. Phys. Chem. A*, **2014**, *118*, 6711.
[36] R. C. Newman, R. E. Pritchard, J. H. Tucker, E. C. Lightowlers, *Phys. B Condens. Matter* **1999**, *273–274*, 164.
[37] S. Sumari, F. Fajaroh, *Mater. Sci. Eng.* **2019**, *515*, 1.
[38] C. Martínez, A. Corma, *Compr. Inorg. Chem. II (Second Ed. From Elem. To Appl.)* **2013**, pp. 103–131.
[39] T. De Baerdemaeker, D. De Vos, *Nat. Chem.* **2013**, *5*, 89.
[40] H. Bluhm, In*Situ Characterization of Thin Film Growth*, Elsevier, Cambridge, UK **2011**, pp. 75–98.
[41] M. Huang, A. Adnot, S. Kaliaguine, *J. Am. Chem. Soc.* **1992**, *114*, 10005.
[42] J. Oenema, J. P. Hofmann, E. J. M. Hensen, J. Zečević, *ChemCatChem* **2020**, *12*, 615.
[43] A. Dane, U. K. Demirok, A. Aydinli, S. Suzer, *J. Phys. Chem. B* **2006**, *110*, 1137.
[44] S. Khaldi, P. Karadan, K. Killi, C. E. M. de Oliveira, R. Yerushalmi, *Chem. Commun.* **2024**, *60*, 11754.
[45] S. Senthilkumar, W. Zhong, M. Natarajan, C. Lu, B. Xu, X. Liu, *New J. Chem.* **2021**, *45*, 705.
[46] B. Sivaranjini, R. Mangaiyarkarasi, V. Ganesh, S. Umadevi, *Sci. Rep.* **2018**, *8*, 8891.
[47] Y. Jiang, E. Yifeng, P. Wei, J. Wang, P. Chen, L. Wang, T. F. Krenzel, X. Tong, *RSC Adv.* **2023**, *13*, 3364.
[48] D. A. Cole, S. Attavar, L. Zhang, *Dev. Surf. Contam. Clean. Second Ed.* **2016**, *1*, 333.
[49] C. Baker, J. L. Gole, J. Brauer, S. Graham, J. Hu, J. Kenvin, A. D. D. Amico, M. G. White, *Microporous Mesoporous Mater.* **2016**, *220*, 44.
[50] T. F. Chaves, H. O. Pastore, P. Hammer, D. Cardoso, *Microporous Mesoporous Mater.* **2015**, *202*, 198.
[51] R. Fang, Q. Sun, P. Zhou, W. Yang, P. Wang, D. W. Zhang, *Nanoscale Res. Lett.* **2013**, *8*, 1.
[52] Q. Huang, Z. Zhao, X. Wang, J. Wang, Y. Sun, X. Li, *J. Mater. Sci.* **2018**, *53*, 6729.
[53] T. Song, Q. Liu, J. Liu, W. Yang, R. Chen, X. Jing, K. Takahashi, J. Wang, *Appl. Surf. Sci.* **2015**, *355*, 495.
[54] M. Kalhor, Z. Zarnegar, F. Janghorban, *Res. Chem. Intermed.* **2020**, *46*, 821.
[55] E. N. Domoroshchina, V. V. Chernyshev, G. M. Kuz, A. V. Dorokhov, L. V. Pirutko, G. V. Kravchenko, R. B. Chumakov, *Appl. Nanosci.* **2018**, *8*, 19.
[56] A. Zainal Abidin, N. H. H. Abu Bakar, E. P. Ng, W. L. Tan, *J. Taibah Univ. Sci.* **2017**, *11*, 1070.
[57] S. Korichi, A. Elias, A. Mefti, A. Bensmaili, *Appl. Clay Sci.* **2012**, *59–60*, 76.
[58] M. A. Moneim, E. A. Ahmed, *Sci. Res.* **2015**, *5*, 68.
[59] W. Mozgawa, M. Król, K. Barczyk, *Chemik* **2011**, *65*, 671.
[60] A. Palomo, A. Ferna, *Microporous Mesoporous Mater.* **2005**, *86*, 207.
[61] L. D. E. Molecular, F. De Ciencias, U. D. L. Andes, *Am. J. Anal. Chem.* **2013**, *2013*, 387.
[62] M. M. Rahman, N. Hasnida, W. B. Wan Nik, *J. Sci. Res.* **2009**, *1*, 285.
[63] M. Król, A. Koleżyński, W. Mozgawa, *Molecules* **2021**, *26*, 342.
[64] M. Król, W. Mozgawa, W. Jastrze, K. Barczyk, *Microporous Mesoporous Mater. J.* **2012**, *156*, 181.
[65] E. Domoroshchina, A. Orekhov, V. Chernyshev, *Res. Chem. Intermed.* **2019**, *45*, 2869.
[66] H. Moldenhauer, I. Díaz-franulic, F. González-nilo, D. Naranjo, *Sci. Rep.* **2016**, *6*, 7.
[67] R. D. Shannon, *Acta Cryst.* **1976**, *A32*, 751.
[68] J. Loeb, *J. Gen. Physiol.* **1920**, *2*, 673.
[69] H. J. Choi, D. Jo, J. G. Min, S. B. Hong, *Angew. Chemie Int. Ed.* **2021**, *60*, 4307.
[70] A. J. W. Physick, D. J. Wales, S. H. R. Owens, J. Shang, P. A. Webley, T. J. Mays, V. P. Ting, *Chem. Eng. J.* **2016**, *288*, 161.
[71] M.-Z. Kim, S. F. Alam, D. Arepalli, A. U. Rehman, W.-Y. Choi, C.-H. Cho, *Nanomaterials* **2021**, *11*, 2113.

[72] S. Sircar, *J. Chem. Soc. Faraday Trans. 1 Phys. Chem. Condens. Phases* **1983**, *79*, 785.
[73] D. H. Kim, *AIChE J.* **1989**, *35*, 343.
[74] G. Rehage, O. Ernst, J. Fuhrmann, *Discuss. Faraday Soc.* **1970**, *49*, 208.
[75] P. Cruz, F. D. Magalhães, A. Mendes, *Chem. Eng. Sci.* **2006**, *61*, 3519.
[76] M. I. Ojovan, W. E. Lee, S. N. Kalmykov, *An Introduction to Nuclear Waste Immobilization*, Elsevier, Amsterdam, Netherlands **2019**, pp. 145–154.
[77] A. Dutta, A. Chanda, R. Chakraborty, *Int. J. Food Eng.* **2008**, *4*, 203.
[78] M. Yuan, K. Lee, D. G. Van Campen, S. Liguori, M. F. Toney, J. Wilcox, *Ind. Eng. Chem. Res.* **2019**, *58*, 926.
[79] Y. Si, X. He, J. Jiang, Z. Duan, W. Wang, D. Yuan, *Nano Res.* **2021**, *14*, 518.
[80] C. L. Hobday, C. H. Woodall, M. J. Lennox, M. Frost, K. Kamenev, T. Düren, C. A. Morrison, S. A. Moggach, *Nat. Commun.* **2018**, *9*, 1.
[81] S. Aydin, C. Altintas, S. Keskin, *ACS Appl. Mater. Interfaces* **2022**, *14*, 21738.